■ Organic Semiconductors

Modulating the Electronic and Solid-State Structure of Organic Semiconductors by Site-Specific Substitution: The Case of Tetrafluoropentacenes

Thomas Geiger,[a] Simon Schundelmeier,[a] Thorsten Hummel,[b] Markus Ströbele,[b] Wolfgang Leis,[b] Michael Seitz,[b] Clemens Zeiser,[c] Luca Moretti,[d] Margherita Maiuri,[d] Giulio Cerullo,[d] Katharina Broch,[c] Jörn Vahland,[e] Karl Leo,[e] Cäcilia Maichle-Mössmer,[b] Bernd Speiser,[a] and Holger F. Bettinger*[a]

Abstract: The properties as well as solid-state structures, singlet fission, and organic field-effect transistor (OFET) performance of three tetrafluoropentacenes (1,4,8,11: **10**, 1,4,9,10: **11**, 2,3,9,10: **12**) are compared herein. The novel compounds **10** and **11** were synthesized in high purity from the corresponding 6,13-etheno-bridged precursors by reaction with dimethyl 1,2,4,5-tetrazine-3,6-dicarboxylate at elevated temperatures. Although most of the molecular properties of the compounds are similar, their chemical reactivity and crystal structures differ considerably. Isomer **10** undergoes the orbital symmetry forbidden thermal [4+4] dimerization, whereas **11** and **12** are much less reactive. The isomers **11** and **12** crystallize in a herringbone motif, but **10** prefers π–π stacking. Although the energy of the first electric dipole-allowed optical transition varies only within 370 cm^{-1} (0.05 eV) for the neutral compounds, this amounts to roughly 1600 cm^{-1} (0.20 eV) for radical cations and 1300 cm^{-1} (0.16 eV) for dications. Transient spectroscopy of films of **11** and **12** reveals singlet-fission time constants (91$\pm$11, 73$\pm$3 fs, respectively) that are shorter than for pentacene (112$\pm$9 fs). OFET devices constructed from **11** and **12** show close to ideal thin-film transistor (TFT) characteristics with electron mobilities of 2×10^{-3} and 6×10^{-2} cm^{2}V^{-1}s^{-1}, respectively.

Introduction

The world we know today has been shaped by the use of electronic devices in our everyday life. The need for miniaturization and adaption to new form factors, allowing for novel and light-weight devices, for example, consumer electronics with foldable displays as seen in the newest smartphone developments or flexible solar cells, cannot be met by silicon-based electronic components because they inherently lack flexibility. For such applications, devices based on organic semiconductors are highly advantageous, given that these can be manufactured using flexible substrate materials.[1,2]

To meet demands, material scientists are highly interested in finding new materials which can be incorporated into such systems, allowing for even better device performances.[3] Acenes, the group of polycyclic aromatic hydrocarbons (PAHs) consisting of linear annulated benzene rings with semiconductor properties and an almost linear correlation between the inverse of the number of rings and the HOMO–LUMO gap,[4] are interesting materials for such applications.[3,5,6] The most commonly used substance from this class of compounds is pentacene because of its good availability and higher stability in comparison with the higher homologues of the series. It has been shown that pentacene is a p-type semiconductor[7,8] with

[a] T. Geiger, S. Schundelmeier, Prof. Dr. B. Speiser, Prof. Dr. H. F. Bettinger
Institut für Organische Chemie, Universität Tübingen
Auf der Morgenstelle 18, 72076 Tübingen (Germany)
E-mail: holger.bettinger@uni-tuebingen.de

[b] T. Hummel, Dr. M. Ströbele, Dr. W. Leis, Prof. Dr. M. Seitz,
Dr. C. Maichle-Mössmer
Institut für Anorganische Chemie, Universität Tübingen
Auf der Morgenstelle 18, 72076 Tübingen (Germany)

[c] C. Zeiser, Jun.-Prof. Dr. K. Broch
Institut für Angewandte Physik, Universität Tübingen
Auf der Morgenstelle 10, 72076 Tübingen (Germany)

[d] L. Moretti, Dr. M. Maiuri, Prof. Dr. G. Cerullo
IFN-CNR, Dipartimento di Fisica, Politecnico di Milano
Piazza Leonardo da Vinci 32, 20133 Milano (Italy)

[e] J. Vahland, Prof. Dr. K. Leo
Dresden Integrated Center for Applied Physics and Photonic Materials
Technische Universität Dresden
Nöthnitzer Strasse 61, 01187 Dresden (Germany)

Supporting information and the ORCID identification number(s) for the author(s) of this article can be found under:
https://doi.org/10.1002/chem.201905843.

a hole mobility of up to 35 cm^{2}V^{-1}s^{-1} in a single crystal at room temperature.[9] For some applications, an n-type semiconductor is desirable, and it could be shown that it is possible to convert the conduction mode of pentacene by introduction of electron-withdrawing groups like fluorine atoms or nitrile groups to the pentacene scaffold.[7,10–13] A very prominent example for the power of fluorine substitution is perfluoropentacene (PFP), in which the full exchange of all hydrogen atoms by fluorine atoms results in a change of charge-transport mechanism from p-type to n-type.[10,14] Since its first synthesis, many properties of PFP have been investigated very extensively.

In contrast, the influence of only partial fluorine substitution at the pentacene scaffold has received less attention. Groundbreaking work on partially fluorinated 6,13-bis(triisopropylsilylethynyl)pentacenes (TIPS-pentacenes) was performed by Anthony et al.[11,15–17] The partially fluorinated derivatives (1,2,3,4-tetrafluoro and 1,2,3,4,8,9,10,11-octafluoro) showed higher hole mobilities than TIPS-pentacene under identical deposition conditions.[11] Bao et al., in contrast, identified partially fluorinated tetracenothiophenes as ambipolar semiconductors with high performance.[18,19] More recently, further experimental evidence that the charge-carrier mobility can be modified by site-specific fluorination and changing the number of fluorine atoms on the pentacene backbone was provided by Wasikiewicz et al.[20] They reported the synthesis of a subgroup of soluble mono- and difluorinated TIPS-pentacenes and found that the 2,10-difluoro isomer reached the highest μ_{Mean} (average mobility) of all compounds they investigated.

In addition to these experimental investigations, there are a number of computational studies on partially fluorinated pentacenes without solubilizing side groups, and some very interesting predictions were made.[21–25] Toyoda et al.[21] were able to show by in silico investigations that the efficiency of electron injection on a Cu(111) surface can be related to the number of fluorine atoms and their respective position in the pentacene backbone. Although pentacene showed the highest efficiency, PFP showed a significantly lower efficiency. This was explained by a larger PFP/Cu(111) distance due to repulsive interactions of the fluorine 2p orbitals with the substrate,[22] as observed by an X-ray standing-wave investigation (2.34 vs. 2.98 Å for PEN and PFP, respectively, on Cu(111)).[26] Toyoda et al.[21] suggested that it could be possible to fabricate interfaces optimal for charge-carrier injection by using pentacenes with a number of fluorine atoms n_F less than or equal to eight. A systematic computational DFT study of symmetrical substituted fluoropentacenes ($n_F = 2$–14) by Lukeš et al.[23] came to the conclusion that charge-carrier mobility is lowest in PFP, whereas 1,4,8,11-tetrafluoropentacene should show the highest mobility of up to 7.30 cm^{2}V^{-1}s^{-1} depending on the dimer configuration used for the calculations. Even though this value looks very promising, the authors cautioned that the relatively high LUMO energy would not be favorable for an n-type semiconductor. Given that charge-carrier mobility is not only affected by the HOMO and LUMO levels, but also relies on efficient through-space coupling between next neighbors, modification of the crystal packaging by fluorine substitution is an impor-

tant factor.[27] The influence of partial fluorination on the packing motifs of a total of fifteen fluorinated rubrene derivatives was impressively shown by Ogden et al.[28]

Although interesting properties for partially fluorinated pentacenes were predicted, this compound class is quite rare and limited to 2-fluoro-, 1,2,3,4-tetrafluoro-, and 2,3,9,10-tetrafluoropentacene. Chow's group synthesized the former two derivatives by thermal decarbonylation from the bridged ketone (Scheme 1a).[29,30] The 2-fluoro derivative was characterized as a p-channel semiconductor,[30] whereas 1,2,3,4-tetrafluoropentacene exhibits ambipolar charge-transport behavior depending on the electrode material used.[29] The Bettinger group obtained 2,3,9,10-tetrafluoropentacene either by thermal removal of a 6,13-etheno bridge using a 1,2,4,5-tetrazine derivative,[31] or by Strating–Zwanenburg reaction,[32] the photoinduced bis-decarbonylation of the 6,13-bridged α-diketone (Scheme 1b).[33] The photochemical conversions usually give higher yields,[34] but losses of substance due to the additional two steps for preparation of the α-diketones have to be taken into account when comparing both methods.

For 2,3,9,10-tetrafluoropentacene, no OFET data are available, but its interfacial properties on metal surfaces were studied extensively.[35–37] The compound shows pronounced nano-rod morphology on Au(110) and charge transfer from the surface, indicating that the chemical modification has impact on the morphology and electronic properties at the molecular and thin-film levels.[35,36] An X-ray standing-wave investigation could quantify the substantial molecular distortion that 2,3,9,10-tetrafluoropentacene is undergoing upon interaction with a Cu(111) surface on an atomic level.[37]

In this work, we describe the synthesis of two new isomers of peripherally substituted tetrafluoropentacenes with a 1,4,8,11- (for which computational predictions were made by Lukeš et al.)[23] and 1,4,9,10-substitution pattern (Scheme 1c) using the 1,2,4,5-tetrazine-induced elimination of the 6,13-etheno bridge. We compare the chemical, electrochemical, and photophysical properties, including singlet-fission dynamics, as well as crystal-structure data and OFET device performance in the series of tetrafluoropentacenes.

Results and Discussion

Synthesis

The precursors used for thermal generation of the fluorinated pentacenes were synthesized by reaction of 5,6,7,8-tetramethylidenebicyclo[2.2.2]oct-2-ene (1)[38,39] with 3,6-difluoroaryne that was generated from 3,6-difluoro-2-(trimethylsilyl)phenyltriflate (2) and CsF (Scheme 2). Single crystals of compound 1 suitable for X-ray crystallography were obtained by slow evaporation of the solvent from a solution in n-hexane (for detailed structural information, see the Supporting Information).

The aryne precursor 2 was prepared using a synthesis published by Tsuchido et al.[40] starting from 2-bromo-3,6-difluorophenol in 26% yield (Scheme 3). Given that this consecutive reaction without isolation of the intermediate 3 leads only to
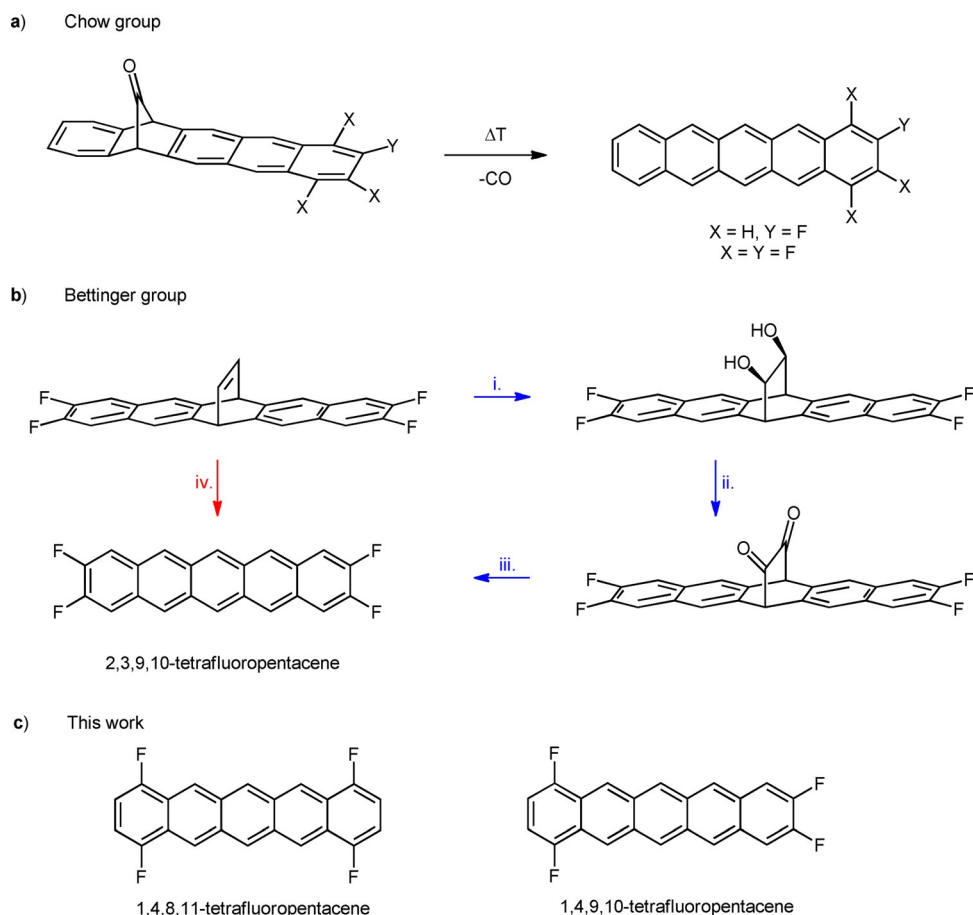
Scheme 1. Previously reported syntheses of partially fluorinated pentacenes by Chow et al. (**a**),[29,30] and Bettinger et al. (**b**; i. OsO₄ (cat.)/NMO, acetone/H₂O, ii. TEMPO/NaOCl, CH₂Cl₂, iii. *hν*, toluene, iv. *n*-pentylether, 180 °C, dimethyl 1,2,4,5-tetrazine-3,6-dicarboxylate, 1.5 min, then 0 °C),[31,33] and the novel tetrafluoropentacene derivatives synthesized and investigated here (**c**).
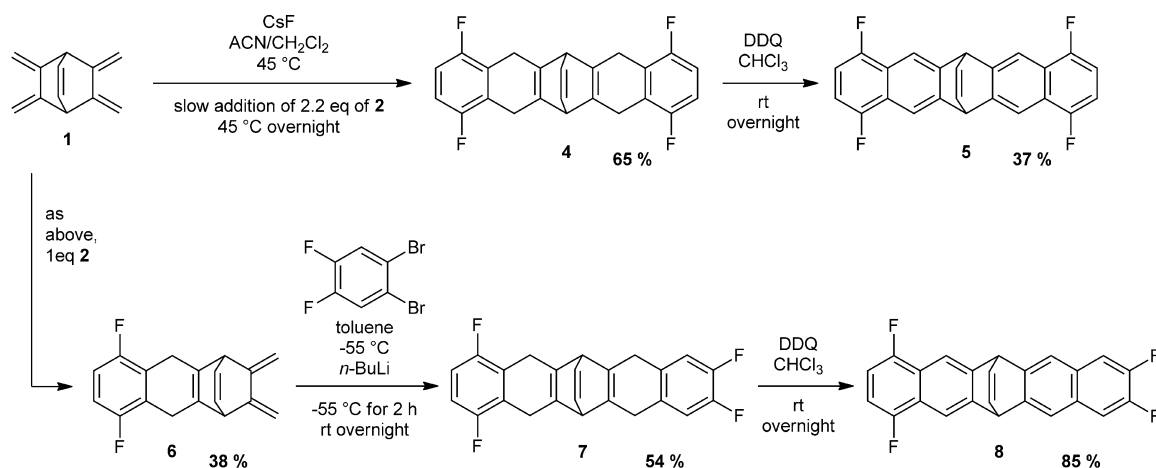
Scheme 2. Synthesis of the mono- (**6**) and bis-adducts (**4** and **7**) of compounds **1** and **2**. The monoadduct **6** is further reacted with 1,2-dibromo-4,5-difluorobenzene to give bis-adduct **7**. Subsequent oxidation with DDQ in CHCl₃ yields the corresponding ethenopentacenes **5** and **8**.

low yields of product with acceptable purity, we isolated compound **3** in 26% yield and applied a triflation strategy using Tf₂O and pyridine as the nucleophilic catalyst.[41,42] After reaction overnight, **2** was isolated in 85% yield. In comparison with the published synthesis[40] the two-step process gives an even lower yield (26% for the direct versus 22% through the two-step method), but the purity of the isolated product was increased significantly.
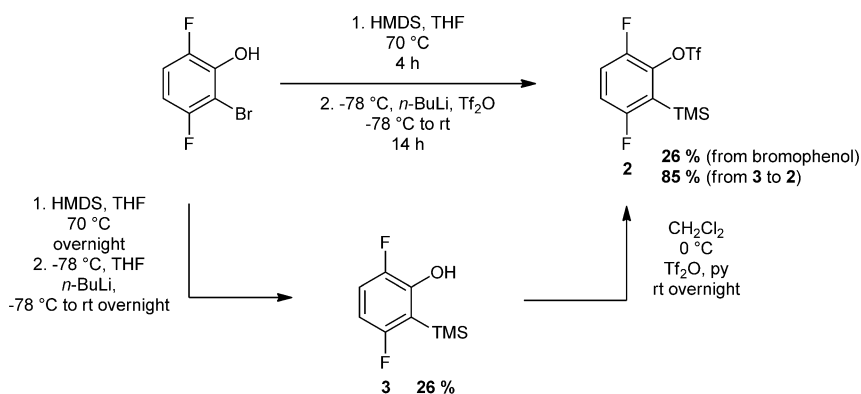
Scheme 3. Synthesis of *o*-TMS triflate (**2**) by one-pot reaction method[40] without isolation of *o*-TMS phenol (**3**) and the two step reaction with isolation of **3**.

Two equivalents of *o*-TMS triflate (**2**) were reacted with anhydrous CsF and **1** in a 1:1 (*v/v*) CH₃CN/CH₂Cl₂ mixture to give bis-adduct **4** (Scheme 2). This compound was subjected directly to 2,3-dichloro-5,6-dicyano-1,4-benzoquinone (DDQ) oxidation in CHCl₃ without further purification. Ethenopentacene **5** was isolated in 37% yield based on the amount of **1** used in the Diels–Alder reaction. For synthesis of the unsymmetrically substituted pentacene precursor, **1** was reacted with only 1 equiv of **2** under otherwise unchanged conditions giving monoadduct **6** in 38% yield. Using our published procedures[31,43] **6** was reacted with 1,2-dibromo-4,5-difluorobenzene giving adduct **7** in 54% yield. After DDQ oxidation, the ethenopentacene **8** was isolated in 85% yield. Single crystals of **5** and **8** suitable for X-ray crystallography were obtained by slow evaporation of a CH₂Cl₂ solution of the respective compounds.

The thermally induced Diels–Alder–retro–Diels–Alder sequence[31] was carried out between the tetrazine (**9**) prepared from ethyl diazoacetate over 5 steps,[44,45] and the respective ethenopentacenes (Scheme 4).

Compared with the previously published procedure,[31] we have introduced minor changes leading to increased yields and purities. Lowering the reaction temperature from 185 to 180°C facilitated the addition of **9** to the reaction mixture because the only mildly boiling solvent does not hinder the addi-

tion of **9** significantly anymore. Additionally, the reactions were carried out multiple times (usually 5–8 times) consecutively in small batches and the reaction products were collected together in a fritted glass funnel under a stream of Ar. The reaction products were washed with degassed *n*-hexane, CH₂Cl₂, and ethyl acetate and dried under vacuum. The revised procedure increased the yield of 2,3,9,10-tetrafluoropentacene (**12**) to 36% compared with the original 12%.[31] 1,4,8,11- (**10**) and 1,4,9,10-tetrafluoropentacene (**11**) were prepared in 30 and 43% yield, accordingly. A computational investigation (M06-2X/6-31G* level of theory) of the reaction sequence (Scheme 4) reveals that the barriers do not strongly depend on the substitution pattern (see the Supporting Information for details). The solubility of **10** and **11** is high enough for measuring ¹H and ¹⁹F NMR spectra in solution at room temperature. In contrast, no ¹³C{¹H} NMR spectra could be obtained, even at 120°C in [D₂]tetrachloroethane as done previously for NMR characterization of **12**. Although **12** is stable at this temperature for an extended period of time, and was indeed crystallized by slow cooling of a hot 1,2,4-trichlorobenzene solution,[33] isomer **10** underwent a reaction. After 3 h of heating to 120°C, all pentacene ¹H NMR signals had completely disappeared (Figure 1) and a new set of three signals (integration ratio 8:8:4) had formed, indicative of a single reaction product with the same
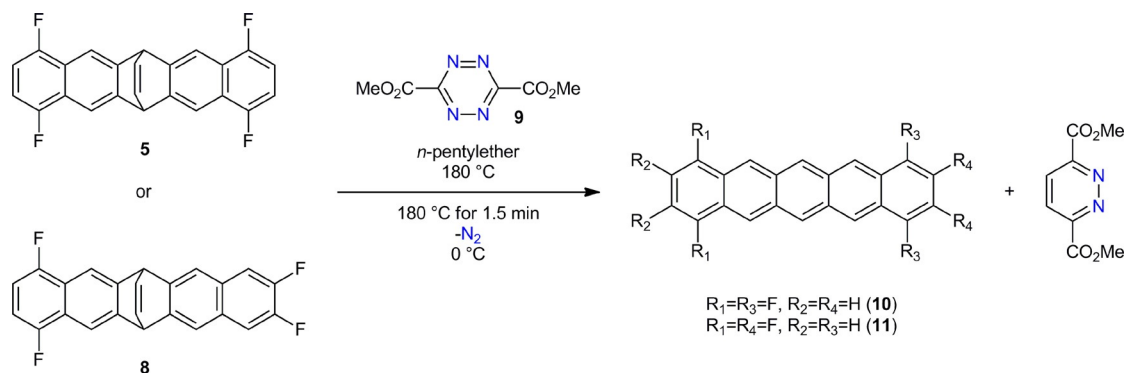
Scheme 4. Thermal synthesis of 1,4,8,11- (**10**) and 1,4,9,10-tetrafluoropentacene (**11**) from the reaction of ethenopentacenes **5** and **8** with dimethyl 1,2,4,5-tetrazine-3,6-dicarboxylate (**9**). Only the relevant reaction products are shown, the byproducts of the reaction have been discussed and characterized in previous publications.[31,33]
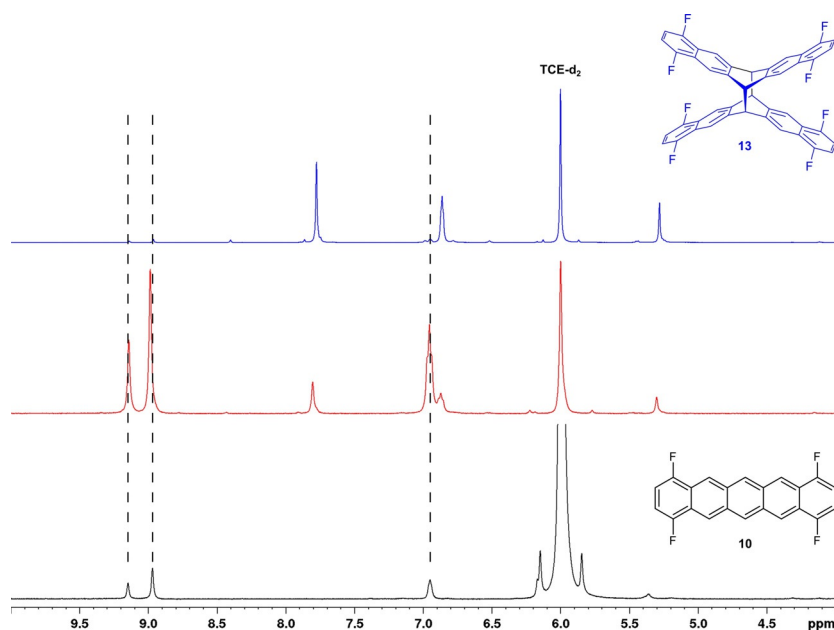
Figure 1. ^{1}H NMR (600 MHz, [D2]tetrachloroethane) spectrum of **10** at rt (black), after 1 h at 120 °C (red, measured at 120 °C) and after 3 h at 120 °C (blue, measured at rt). The vertical dashed lines indicate the signals of **10**. Due to different temperatures at which the spectra were acquired and the fact that the spectra are scaled for better visual comparability the signal intensities are not directly quantitatively comparable.

symmetry. Correlation of chemical shifts with data for pentacene endoperoxide (PcEP),[46] an authentic sample of dianthracene prepared following our general method for preparation of substituted dianthracenes,[47] the thermal dimer of 1,2,3,4-tetrafluoropentacene,[29] and diheptacene[48] (see Supporting Information, Table S1) strongly indicates formation of the covalent dimer **13**.

Mass spectrometric investigation of **13** was precluded due to its instability under electron-impact (EI) conditions. Similar to the observations we have made investigating anthracene dimers,[47] only the mass of the monomer was detected, exhibiting the same fragmentation pattern as an authentic sample of the monomer. Given that the material is too insoluble, electrospray ionization (see the Supporting Information) could not be employed. For the same reason, no single crystals could be grown from solution for further structural elucidation, but a complete assignment of signals was possible using 2D NMR techniques (Figure 2).

Thermal dimerization reactions of pentacene derivatives bearing substituents on the terminal rings have been reported before.[29,49,50] Although orbital-symmetry forbidden according to the Woodward–Hoffmann rules, the thermal [4+4] cycloaddition reaction was rationalized by consideration of packing motifs in the crystal structure as well as by molecular dynamics calculations.[50] It was suggested that a π–π stacking arrangement in the crystal is able to facilitate the solid-state dimerization by pre-aligning the reaction partners.[50] A comparison of the crystal structures of **10**–**12** likewise shows different packing motifs (Figure 3). In comparison with **10**, compound **11** is thermally more stable, because heating for the same period of time at 120 °C shows a slower buildup of presumably dimer signals; the dimers of **11** were not isolated.
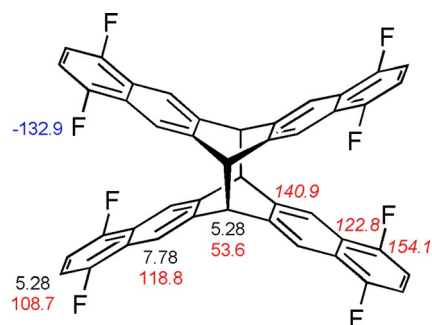
Figure 2. Full signal assignment based on 2D NMR for the thermal dimer **13** of 1,4,8,11-tetrafluoropentacene (**10**) generated by heating the monomer in [D2]tetrachloroethane to 120 °C. [1]H (black), [13]C{[1]H} (red), [19]F (blue). Shifts of quaternary carbon atoms are denoted in italics.

X-ray analysis

Due to the thermal dimerization, crystals of **10** and **11** were not grown from hot solutions as done for **12**, but by sublimation. The samples were fused into homemade two-chamber quartz ampoules (length = 14 cm, inner diameter = 0.7 cm, V = 6.2 cm^3) under vacuum. The ampoule was placed into a homemade tube furnace and heated to 80 °C with a heating and cooling rate of 2 °C min^{-1}. The powder was placed at one end of the ampoule exposed to 80 °C, whereas the other end was left at room temperature. After five days, single crystals of **10** and **11**, suitable for X-ray crystallography measurements were collected at the colder side of the ampoule (Table 1, for detailed crystallographic information see the Supporting Information). The carbon skeleton of **10** shows bond-length alternation between 1.33 and 1.44 Å (Figure 3a), the same range is also found in **11** (Figure 3d). The C−F bond lengths range be-
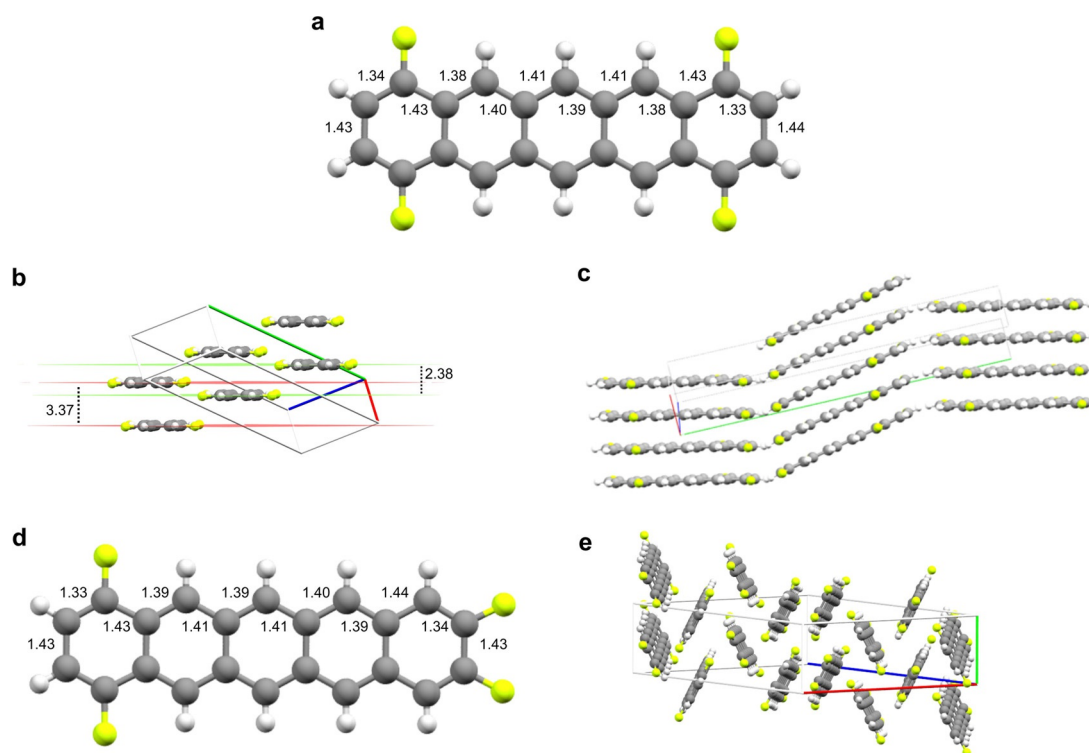
Figure 3. Molecular structure of **10** and **11** in the single crystal. Molecular structures with alternating C—C bond patterns (**a/d**), staircase motif found within the crystal of **10** (**b**) with intercolumn and interplanar distances, out of plane tilting (**c**) and the herringbone-like crystallization motif of **11** (**e**) are shown. Distances are given in Å.

tween 1.36 and 1.37 Å in **10**, whereas the C—F bond lengths in **11** are shorter (1.34–1.36 Å). These values are similar to the ones found in **12**[33] and PFP.[10] The closest intermolecular F—F contacts in the crystal packing of **10** have a distance of 3.34 Å. Although **12**,[33] pentacene, and PFP[10] crystallize in the typical herringbone pattern, **10** crystallizes in a staircase structure which is roughly oriented along the crystallographic c axis (Figure 3b). These molecular planes have an offset of 2.38 Å and the molecules in adjacent layers are shifted 6.4 Å sideways. This staircase motif is disrupted along the b axis by a 24.6° out-of-plane tilt of every second molecular column (Figure 3c). Inside individual molecular columns, the molecules have a vertical distance of 3.37 Å and show π–π stacking. In the crystal packing of **11**, which adopts the herringbone pattern, the closest intermolecular F–F contacts have a distance of 2.91 Å and are therefore significantly shorter than in the crystal packing of **10**. The interaction in this case involves the fluorine atoms in the 1,4-positions of a pentacene molecule and the fluorine atoms in the 9,10-positions of a neighboring pentacene molecule.

Absorption and photoluminescence spectroscopy in solution

The purple-colored solutions in degassed CH_2Cl_2 show the typical vibrational progression (1411 cm^{-1} for **10**; 1406 cm^{-1} for **11**) of the pentacene p-band (Figure 4). Absorption and emission spectra are roughly symmetrical with respect to the 0–0

transition. The excitation spectra contain every band present in the absorption spectra; hence the fluorescence spectra are independent of the excitation wavelength and show emission at 582/632 (**10**) and 579/624 nm (**11**). Overall, the position of the p-band experiences a bathochromic shift (0.02–0.03 eV) from **12** over **11** to **10**. The α bands follow the same trend, but the shift is smaller. The Stokes shift increases from 189 cm^{-1} in **12**[33] to 327 (**10**) and 334 cm^{-1} (**11**), respectively.

The triplet energies of **10**–**12** were measured at 77 K in CD_2Cl_2 and are similar for the three isomers (Table 1, Supporting Information Figures S35–37). Most importantly, the essential requirement for singlet fission, $E(S_1) \geq 2E(T_1)$, is fulfilled for each isomer.

Molecular electrochemistry

The electrochemical redox processes associated with **12** have already been described recently,[33] and are briefly summarized here. The radical cation and anion, as the one-electron oxidation and reduction products of **12**, are generated in a reversible or quasi-reversible electron transfer, respectively, at a Pt electrode in 1,2-dichlorobenzene. For scan rates v down to 0.1 Vs^{-1}, in cyclic voltammetry, follow-up reactions are absent (chemical reversibility) and the oxidation and reduction formal potentials of **12** are easily accessible. A second oxidation signal appears very close to the positive limit of the potential window and was not analyzed in detail.[33] The cyclic voltammograms of **10** and **11** (Figure 5), starting at the rest potential

Table 1. Overview over unit cell data, HOMO/LUMO levels (calculated at the B3LYP/6–311 + G** level of theory), formal oxidation and reduction potentials[a,b] from CV measurements and data for the S_1 and T_1 states obtained from optical spectroscopy in solution. Data for 1,2,3,4-tetrafluoropentacene is taken from Chien et al.,[29] for blank spaces no data is available.

	10	11	12	1,2,3,4-Tetrafluoropentacene[29]
Crystallography				
crystal system	monoclinic	monoclinic	triclinic	
space group	$P2_1$	$P2_1/n$	$P\bar{1}$	
unit cell dimensions	$a = 3.7815(2)$, $\alpha = 90°$	$a = 18.1971(11)$, $\alpha = 90°$	$a = 6.7171(8)$, $\alpha = 100.606(4)°$	
	$b = 27.642(2)$, $\beta = 93.428(5)°$	$b = 5.9311(4)$, $\beta = 92.233(5)°$	$b = 7.6452(9)$, $\beta = 94.579(4)°$	
	$c = 6.9428(5)$ Å $\gamma = 90°$	$c = 26.6590(16)$ Å $\gamma = 90°$	$c = 14.3038(18)$ Å $\gamma = 98.384(4)°$	
Z	2	4	2	
Calculations				
LUMO [eV]	−3.21	−3.17	−3.13	−2.61[c]
HOMO [eV]	−5.39	−5.38	−5.36	−5.17[c]
LUMO–HOMO [eV]	2.18	2.21	2.23	2.56
Electrochemistry				
E^0_{ox} [V]	+0.539	+0.470	+0.402[d]	+0.46[e]
E^0_{red} [V]	−1.663	−1.739	−1.817[d]	−1.67[e]
ΔE^0 [V][f]	2.202	2.209	2.219	2.13
Optical spectroscopy				
S_1 state				
p band	462, 494, 531, 574	459, 490, 526, 568	455, 485, 520, 561	465, 497, 532, 574
α band [nm]	394, 426	400, 425	398, 422	
β band [nm]	328, 343	327, 344	325, 341	
S_1 lifetime [ns][g]	17.06 (98.6%), 65.76 (1.37%)	10.09 (98.5%), 55.49 (1.5%),	8.88 (57.3%), 16.4 (42.7%)	
T_1 state emission [nm][h]	1328	1336	1325	

[a] At Pt in 0.1 M nBu$_4$PF$_6$/1,2-dichlorobenzene as mid-point potential from oxidation and reduction peak potentials in cyclic voltammograms. [b] From chemically reversible cyclic voltammograms; maximum experimental range of scan rates: 0.02 V s$^{-1} \leq v \leq 5$ V s^{-1}. [c] Calculated at the M06/6-31G* level of theory. [d] Values differ slightly from the previous measurement[33] and are based on additional data for conditions given in footnote [a]. [e] $^{ox}E_{1/2}$ and $^{red}E_{1/2}$ in 0.1 M nBu$_4$PF$_6$/CH$_2$Cl$_2$. [f] $\Delta E^0 = E^0_{ox} - E^0_{red}$. [g] Determined at 77 K in 2-Me-THF. Decay curves were fitted as biexponential decays, for more details see the Supporting Information. [h] T_1 lifetimes could not be determined at 77 K in CD$_2$Cl$_2$.

and spanning the positive and negative potential regions separately, show a similar general behavior. However, more quantitative analyses of the current potential curves indicate some subtle differences.

In the positive potential region (all potentials are reported versus an external ferrocene/ferrocenium standard), the re-reduction peak of tetrafluoropentacene **11** is considerably less intense as compared to the oxidation peak at smaller scan rates. This results in a peak current ratio I^{red}_p/I^{ox}_p (calculated according to Nicholson)[51] of less than unity. Only for the largest scan rate used ($v = 5$ V s^{-1}), I^{red}_p/I^{ox}_p approaches unity, indicating that a follow-up reaction of the primary oxidation product occurs and is suppressed only at short time scales (large v).
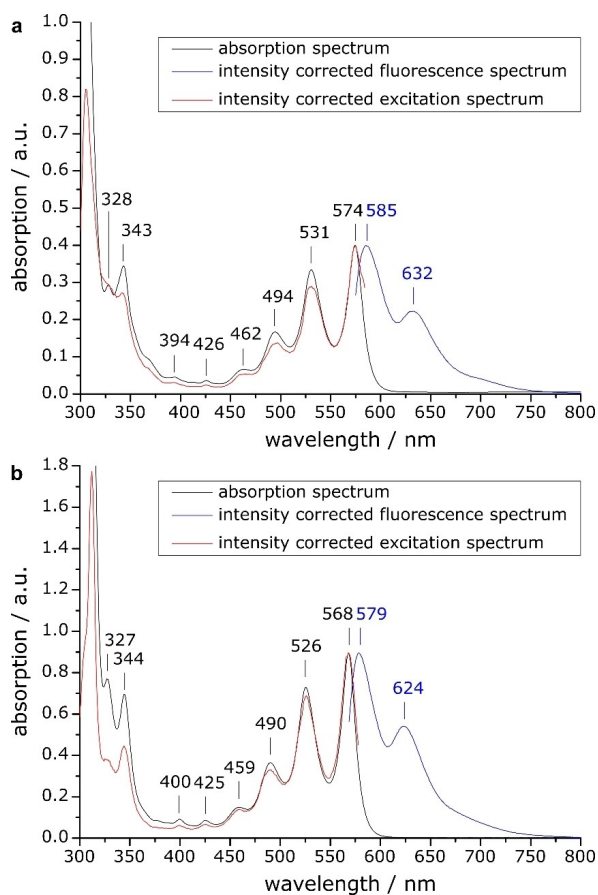
The peak-potential separation ΔE_p at short time scales is around 70 mV, close to the so-called reversible value of 58 mV for a one-electron transfer reaction. We thus conclude that **11** is oxidized to a radical cation **11$^{+\bullet}$**. The observation that ΔE_p is slightly increasing with v for 1 V s$^{-1} \leq v \leq 5$ V s^{-1} indicates the beginning of quasi-reversibility (influence of electron-transfer kinetics). Nonetheless, the peak current is proportional to the square root of v, as expected for voltammograms of diffusing (rather than adsorbed) redox-active species. The formal potential E^0 for this oxidation step is calculated as the mid-point potential from the peak potentials in cyclic voltammograms at $v \geq 0.5$ V s^{-1} (Table 1). The reduction of **11** does not show any

evidence of follow-up reactions. Instead, again, some degree of quasi-reversibility is indicated. The ΔE_p values (≈ 80 mV) suggest formation of a radical anion **11$^{-\bullet}$** through a one-electron reduction.

Most of these mechanistic features were also observed for compound **10**. The primary oxidation product undergoes a follow-up reaction that is somewhat slower than for **11$^{+\bullet}$**, as indicated by the peak–current ratio. The peak-potential difference is ≈ 70 mV with little increase for $v = 2$ V s^{-1} or higher (one-electron transfer to form **10$^{+\bullet}$**). The oxidation peak current increases proportionally to $v^{1/2}$, again showing the redox species to be diffusing rather than being adsorbed. In a similar way, the data are analyzed for the reduction process of **10**, and the analysis shows the chemically and electrochemically reversible formation of **10$^{-\bullet}$** on the time scale of the experiments (E^0 data, see Table 1).

Apart from the determination of the E^0, for **10**, we support the assumption of a follow-up reaction of the radical cation by simulation of the cyclic voltammograms (Figure 6). We assume a first-order reaction of **10$^{+\bullet}$** and use a single set of reaction parameters for the optimal fitting of voltammograms at different scan rates. Thus, a rate constant $k = 0.25$ s^{-1} for the follow-up reaction is estimated, corresponding to $t_{1/2} \approx 2.8$ s.

A further observation, which will not be discussed here in more detail, is the occurrence of a second, irreversible oxida-

Figure 5. Cyclic voltammograms of **10** (**a**) and **11** (**b**) recorded in 0.1 M nBu$_4$PF$_6$/1,2-dichlorobenzene at a Pt disk electrode; **a.** $v = 0.2$ V s^{-1}, $c = 0.42$ mM, **b.** $v = 0.2$ V s^{-1}, $c = 0.38$ mM; the arrows indicate the initial scan directions.
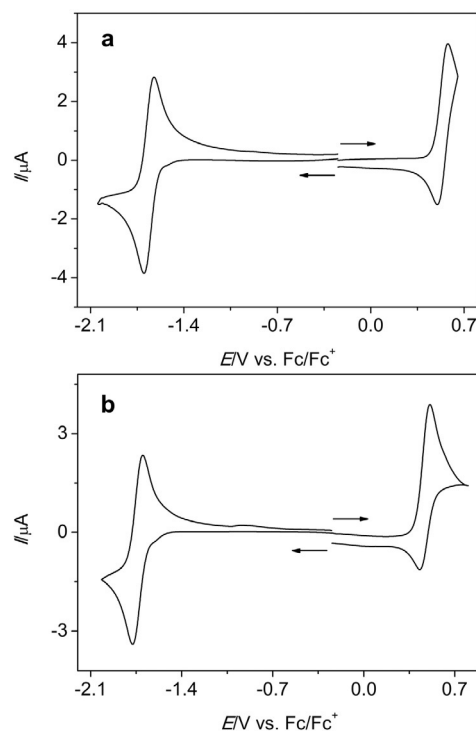
Figure 4. Absorption, fluorescence, and excitation spectra of **10** (**a**, $\lambda_{ex} = 574$ nm, excitation spectrum observed at $\lambda_{em} = 585$ nm) and **11** (**b**, $\lambda_{ex} = 568$ nm, excitation spectrum observed at $\lambda_{em} = 579$ nm) in CH$_2$Cl$_2$.

tion peak for **10** above +0.9 V (Supporting Information, Figure S39). This is not present during the first potential cycle, but its intensity increases during subsequent voltammetric cycles. The signal disappears after polishing the electrode and reappears in the following potential cycles. Most likely, the first cycle on a freshly polished electrode leads to an irreversible modification of the Pt surface.

The formal redox potentials E^0 for oxidation and reduction of the tetrafluoropentacenes (Table 1) decrease to less positive or more negative values in the order **10**→**11**→**12**. The change of the substitution pattern results in an overall shift of approximately 140 mV. We refrain here from estimating orbital energies from the E^0 for reasons discussed in the Supporting Information. However, the difference of the formal potentials ΔE^0 is almost constant over the series with a change of only 17 mV for all compounds. Although these properties are not strictly comparable, the observation of similar values for the ΔE^0 of the compounds is in agreement with the behavior of the S$_1$ maxima obtained from the optical absorption spectra and the HOMO and LUMO energies and energy gaps computed at the B3LYP/6–311+G** level of theory (Table 1).

The comparison with values for pentacene and 2,3,9,10-tetrafluoropentacene (**12**) shows a decrease in the energy gap from 2,3,9,10-tetrafluoropentacene (**12**) to **10** which is in

agreement with the observed bathochromic shift of the p-bands. The decrease in energy gaps almost exclusively arises from the stabilization of the LUMO by up to 0.09 eV, whereas the HOMO energies throughout the series experience a stabilization of only 0.03 eV. The computed HOMO–LUMO energy gaps for **10** and pentacene differ by only 0.01 eV, the same difference is obtained when comparing the transitions of lowest energy (577 nm in pentacene versus 574 nm in **10**).
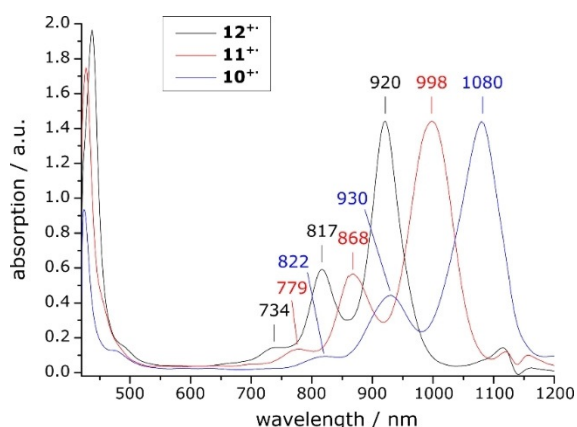
Acene radical cations

Radical cations of both pentacenes were generated by dissolving small samples in a 2 M solution of methanesulfonic acid (MSA) in nitrobenzene under ambient conditions.[33] The oxidation leads to bands in the NIR range (Figure 7). As observed previously for **12**$^{+\bullet}$,[33] the characteristic absorptions of **10**$^{+\bullet}$ and **11**$^{+\bullet}$ disappear within a few hours under buildup of new broad bands with two isosbestic points in each case (Supporting Information, Figures S40 and S41). A comparison of all three radical cation species shows that the energy strongly depends on the substitution pattern. Although **12**$^{+\bullet}$ absorbs at the shortest and **10**$^{+\bullet}$ at the longest wavelength, the difference between these transition energies amounts to 0.2 eV. For the band at 430 nm this effect is reversed, but is not as pronounced (Supporting Information, Table S3). Calculation of the excited-state energies at the UB3LYP/6–311+G** level of theory agrees with the bathochromic shift in the series **12**$^{+\bullet}$ < **11**$^{+\bullet}$ < **10**$^{+\bullet}$, and deviates by 0.05 eV or less (Table S3).
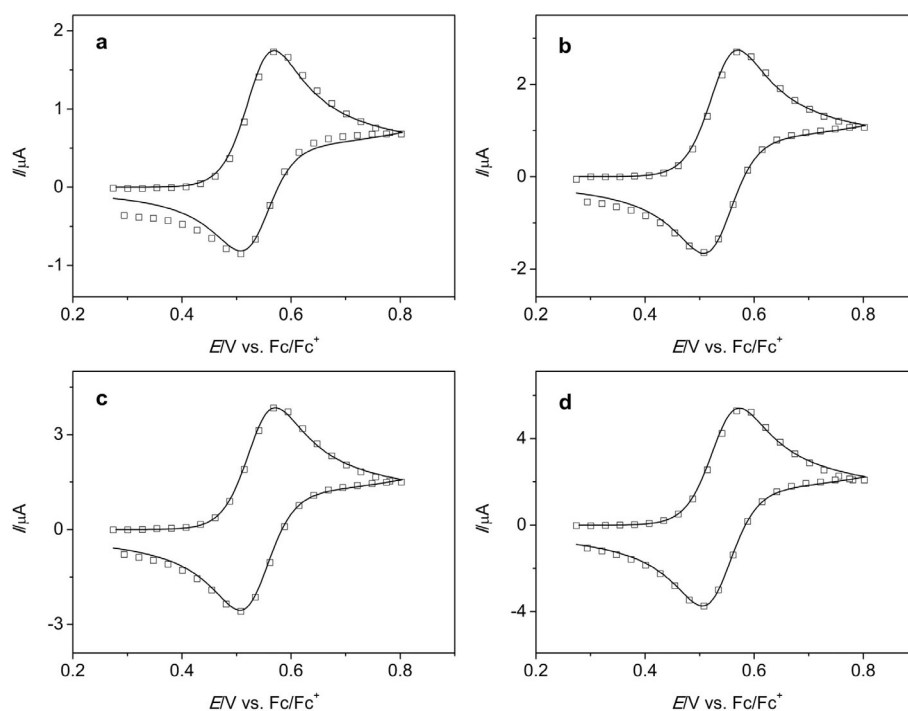
Figure 6. Experimental (symbols) and simulated (lines) cyclic voltammograms of **10** at Pt in 0.1 M nBu$_4$PF$_6$/1,2-dichlorobenzene; $c = 0.70$ mM, $v = 0.2$ (**a**), 0.5 (**b**) 1.0 (**c**), 2.0 V s^{-1} (**d**); parameters for simulation: temperature $T = 298$ K, electroactive area $A = 0.062$ cm^2, $E^0 = 0.539$ V, transfer coefficient $\alpha = 0.5$, electron-transfer rate constant $k_s = 0.05$ cm s^{-1}, diffusion coefficient $D = 1.5 \times 10^{-6}$ cm s^{-1}; to simulate an essentially irreversible chemical process, the equilibrium constant for the follow-up reaction was set to 10^{10}, with a rate constant $k = 0.25$ s^{-1}.


Figure 7. Comparison of the absorption spectra of the radical cations of **10$^{+\cdot}$**, **11$^{+\cdot}$**, and **12$^{+\cdot}$** in 2 M MSA/nitrobenzene solution. The spectra of **10$^{+\cdot}$** and **11$^{+\cdot}$** are scaled in intensity for better comparability.

The radical cations in 2 M MSA/nitrobenzene were also investigated by EPR spectroscopy (Figure 8). Spectra simulation was performed starting from values obtained by computation of the hyperfine coupling constants using the UB3LYP functional and Barone's[52] EPR-III basis set. The simulation resulted in $a_{H_{6/13}} = 4.86$, $a_{H_{7/12/14}} = 3.16$, $a_{F_{1/4/8/11}} = 2.21$, and $a_{H_{2/3/9/10}} = 1.18$ G for **10$^{+\cdot}$** (Table 2). Towards the periphery, the hyperfine couplings decrease, indicating that the electron is predominantly located at the central ring. The values found compare well with the ones already determined for **12$^{+\cdot}$**,[33] which shows that this symmetric substitution pattern does not influence the lo-

cation of the electron. Simulation of the spectrum of **11$^{+\cdot}$** resulted in $a_{H_{6/13}} = 4.34$, $a_{H_{7/12}} = 3.56$, $a_{H_{5/14}} = 2.65$, $a_{F_{1/14}} = 2.34$, $a_{H_{8/11}} = 1.49$, $a_{H_{2/3}} = 1.04$, and $a_{F_{9/10}} = 0.61$ G. In this case, the less symmetric fluorination pattern significantly influences the hyperfine coupling constants. Although the coupling constants decrease in both directions towards the periphery, the values for the 1,4-fluorinated naphthalene subsystem are slightly larger, showing that the electron is more strongly coupling to the protons and fluorine nuclei in this subunit. This is an indication that the electron is in closer spatial proximity to these coupling partners and therefore the probability density of the electron is shifted towards the 1,4-subsystem by the substitution. This is in agreement with the computed shapes of the HOMOs of **10$^{+\cdot}$** and **11$^{+\cdot}$** and also the spin densities (Supporting Information, Figures S45 and S46).

Acene dications

Solutions of the dications were prepared by dissolving samples of the corresponding pentacenes in oleum (20–30% free SO$_3$), yielding deeply colored solutions. These were used for acquisition of NMR spectra or, in diluted form, for the UV/Vis experiments. To prevent rapid H/D exchange, an external D$_2$SO$_4$ standard was used for the NMR experiments because spectra cannot be acquired in the deuterated solvent alone, as reported previously for **12^{2+}**.[33] The oxidation does not involve the evolution of H$_2$ or HD gas because no signals in the range expected for these species were found in the ^{1}H or ^{2}D spectra
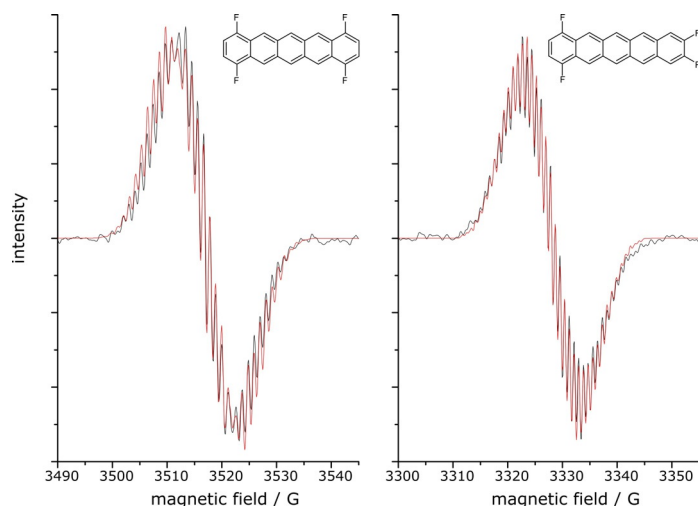
Figure 8. EPR spectra of **10**[+•] (left) and **11**[+•] (right) in 2 M MSA/nitrobenzene. Experimental spectrum in black, simulation in red.

changes in the proton spectra occur at positions attached to the fluorinated rings. Furthermore, starting from the carbon atoms of the innermost ring, every second carbon atoms experiences major deshielding in the dications. The carbon atoms adjacent to the fluorine atoms are additionally deshielded by the inductive effects of fluorine. We explain this chemical shift alternation by the predominant localization of the positive charges on these respective carbon atoms. Adjacent atoms are only deshielded to minor extent in this picture, which is indeed the case.

Transient-absorption spectroscopy of thin films of tetrafluoropentacenes

We also investigated the photophysics of thin films of **11** and **12** by transient-absorption (TA) spectroscopy given that partially fluorinated TIPS-pentacenes

Table 2. Comparison of the values for hyperfine coupling constants (in G) derived from EPR simulation and the values calculated at the UB3LYP/EPR-III level of theory.

	10[+•]				**11**[+•]	
	sim.	calcd			sim.	calcd
$H_{6/13}$	4.86	4.53		$H_{6/13}$	4.34	4.82
$H_{5/7/12/14}$	3.16	3.45		$H_{7/12}$	3.56[b]	3.59
$F_{1/4/8/11}$	2.21[a]	3.09		$H_{5/14}$	2.65[b]	3.64
$H_{2/3/9/10}$	1.18	1.07		$F_{1/4}$	2.34[a]	3.20
				$H_{8/11}$	1.49	1.31
				$H_{2/3}$	1.04	1.13
				$F_{9/10}$	0.61[a]	1.04

[a] Significant deviations for sim. and calcd hyperfine coupling constants for fluorine have been reported for other fluorinated acenes.[53] [b] Interchanging these values does not change the correlation (R^2) between simulation and experimental spectrum in a significant way.

Figure 9. Comparison of the absorption spectra of **10**²⁺, **11**²⁺, and **12**²⁺ in oleum. The spectra of **10**²⁺ and **11**²⁺ are scaled for better comparability. A distinct bathochromic shift of the absorption bands above 700 nm is visible.
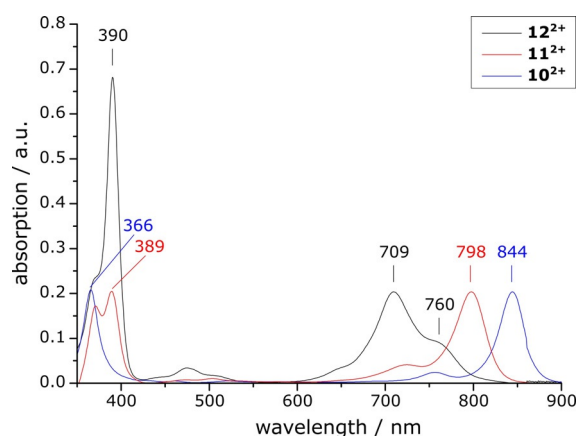
when the reaction was performed in a sealed J-Young NMR tube.

The form of the absorption bands (Figure 9) of the newly prepared dications resemble the spectrum of the pentacene dication[33] rather than **12**²⁺ which shows an inverted intensity profile of the bands above 700 nm. The reason for this behavior is unknown and **12**²⁺ is the only compound in the sequence with an absorption spectrum that does not follow this general rule. The transitions of lowest energy were calculated at the B3LYP/6–311＋G** level of theory (Supporting Information, Table S3) and compare well with the experimentally obtained values, overestimating the energies by up to 0.25 eV.

Using 2D NMR techniques and spectra correlation, full signal assignment is possible for both dications (Figure 10). The ¹H, ¹⁹F and ¹³C{¹H} NMR spectra of **11**²⁺ can be interpreted as an almost exact superposition of the spectra of **10**²⁺ and **12**²⁺. This is also the case for all precursors and the neutral tetrafluoropentacenes themselves. Comparison with the chemical shifts of the neutral molecules shows that the greatest

were shown to be relevant for singlet fission (SF).[54,55] This photophysical process converts an excited singlet state into two triplet states on neighboring molecules[56] and has received increasing attention due to its potential to boost solar cell efficiencies above the Shockley–Queisser limit.[57] It proceeds via a triplet pair state ¹(TT) in which the two molecules involved are already in their triplet state, but the overall character of the state is still a singlet.[58] Most importantly, the triplets are electronically coupled and spin-entangled.[59] A promising approach to optimize SF efficiencies for applications is chemical modification, which in turn often affects molecular arrangement.[60,61] Due to the coupled triplet-pair state, formation of which is a crucial step in the SF process, SF is highly sensitive to changes in molecular packing[60–66] and small modifications in the orbital overlap can be used to tune SF.[62]

Given that the molecular arrangement in thin films often differs from the single-crystal phase, we measured the structure of 80 nm thick films using X-ray reflectivity (Figure 11). Penta-
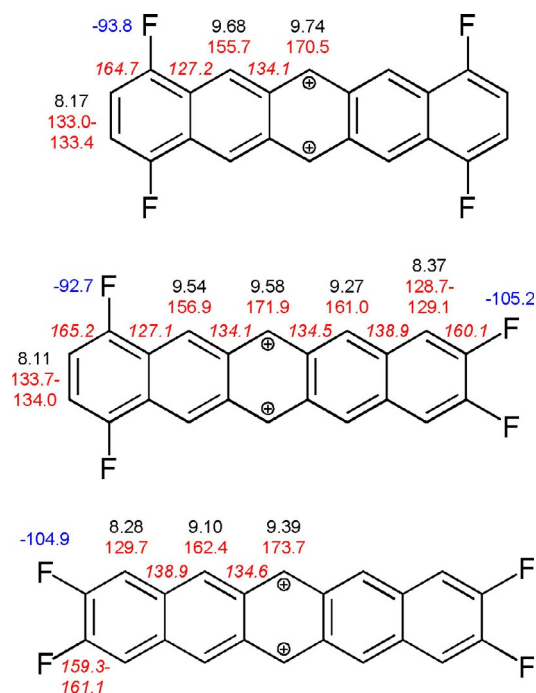
Figure 10. Signal assignment for **10²⁺** (top), **11²⁺** (middle), and **12²⁺** (bottom)[33] measured in oleum with external D_2SO_4 standard. [1]H shifts (black), [13]C{[1]H} shifts (red), ^{19}F shifts (blue). Chemical shifts in ppm, values for quaternary carbon atoms in italics. Assignment of the ^{19}F signals for **11²⁺** is based on correlation with the spectra of the other two isomers.
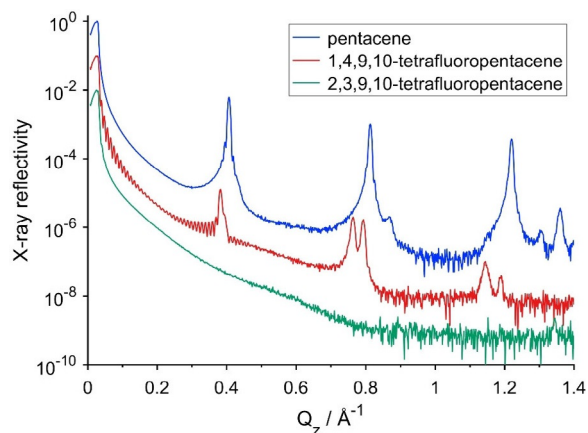
Figure 11. X-ray reflectivity scans of the thin films of pentacene, 1,4,9,10-tetrafluoropentacene (**11**) and 2,3,9,10-tetrafluoropentacene (**12**).

cene shows intense Bragg reflections as expected, because it grows in polycrystalline fashion on SiO_2.[67] The Bragg peak position indicates an out of plane lattice spacing of $d = 15.40$ Å, corresponding to the thin-film phase of pentacene.[67] As expected for film thickness above 40 nm, Bragg peaks of the bulk phase[68] ($d = 14.46$ Å) are observed at $q_z = 0.87$ and $q_z = 1.30$ Å^{-1}. The Bragg peak at $q_z = 1.36$ Å^{-1} is assigned to a small fraction of flat-lying molecules.
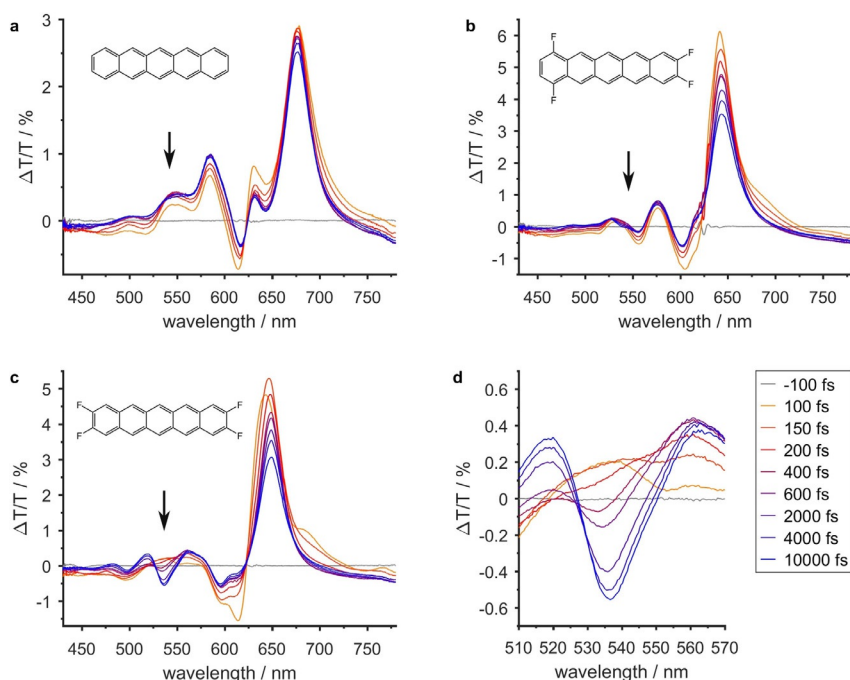
For the thin film of 1,4,9,10-tetrafluoropentacene (**11**) we observe pronounced Kiessig fringes, indicating a low roughness of the film, and two series of Bragg peaks, indicating the pres-

ence of two polymorphs with out-of-plane lattice spacings of $d = 16.46$ and $d = 15.85$ Å, respectively, in the film. We assign these polymorphs to a thin film ($d = 16.46$ Å) and a bulk phase ($d = 15.85$ Å) as observed for pentacene. Interestingly, 2,3,9,10-tetrafluoropentacene (**12**) does not exhibit Bragg peaks in the thin film, indicating an amorphous growth. The weak peak at $q_z = 1.35$ Å^{-1} might arise from a small fraction of crystalline domains within the film, where the molecules are flat lying.

The TA spectroscopy experiments were performed exciting the films (for the absorption spectra of the thin films see the Supporting Information, Figure S38) with 70 fs pulses at 620 nm and probing with a white light continuum covering the 430–780 nm wavelength range. The TA spectra of pentacene (Figure 12 a) agree with previous reports.[69] The TA-spectra of **11** and **12** (Figure 12 b/c) show features similar to pentacene, in particular regarding the photoinduced absorption (PA) bands below a probe wavelength of 500 nm and above a probe wavelength of 720 nm. The decay of the PA band < 500 nm and the rise of the PA band > 720 nm occur in parallel with time constants shorter than 200 fs, similar to pentacene. For compound **12** we reproducibly observe an additional spectral feature at 540 nm, which starts to build up after 200 fs.

A global analysis[70] of these measurements (Figure 13) reveals that there are three spectroscopically distinguishable species in **12**, whereas the TA-data for pentacene and **11** can be analyzed using only two species. Correspondingly, the data can be fitted with a 2-step (3-step) kinetic model, respectively, involving transitions between two species in pentacene and **11** and three species in **12**. The time constant of the transition from species 1 to 2 is 112 ± 9 (pentacene), 91 ± 11 (**11**) and 73 ± 3 fs (**12**). The population of the second species in pentacene and **11** remains constant on the 1 ns experimental observation window, whereas the second species in **12** decays to a third species with an intermediate time constant of 870 ± 140 fs.

The first and second species in pentacene have been assigned to singlets and triplets, respectively[69,71,72] and, therefore, the time constant of the transition from species 1 to 2 in pentacene corresponds to the singlet-fission time constant. For **11**, both, the PA signal at wavelengths below 500 nm and the PA signal at wavelengths above 720 nm have a spectral shape similar to the signals in pentacene, allowing us to assign them to the spectral features of singlets and triplets, respectively, and the conversion time to the SF time constant. In **12**, the first species can again be assigned to singlets. The spectroscopic signatures of the second and third species are very similar and both do not show pronounced intensity at short wavelengths below 500 nm, but a negative feature at wavelengths above 720 nm, which we assign to the characteristic triplet PA, similar to pentacene. Thus, the second and third species of **12** seem to be related to triplets. It is interesting that these two triplet signatures evolve into each other and do not arise independently in the TA data. Thus, it is unlikely that they are caused by exciton migration to low-lying sites within the film, but they have to have the same origin. We believe that the details of the SF process could provide a possible explanation for

Figure 12. Transient absorption spectroscopy data of the three compounds pentacene (a), 1,4,9,10-tetrafluoropentacene (**11**, b) and 2,3,9,10-tetrafluoropenta-cene (**12**, c). d) Zoom into the wavelength region showing the ^{1}(TT)-signature of c.
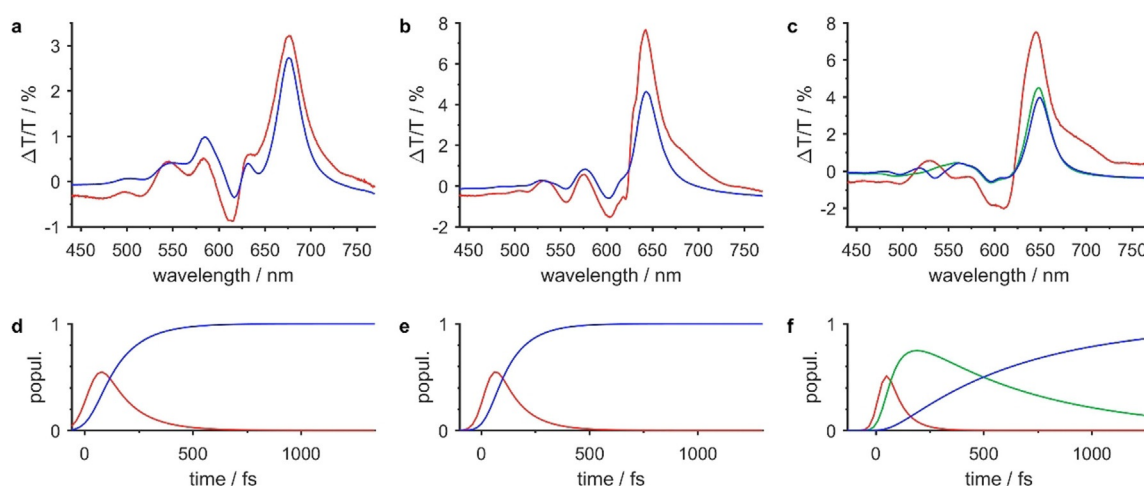
Figure 13. Global analysis of the TA spectroscopy data shown in Figure 12. a)–c) Resulting evolution associated spectra (EAS), d)–f) corresponding singlet and triplet population.

the presence of a third species. During a SF process two neighboring, spin-entangled triplet excitons are formed, which can be electronically coupled resulting in a multiexciton state ^{1}(TT).[58,59] This electronic coupling can be overcome by spatial separation of the triplets into T_1+T_1 via a spin-entangled, but electronically decoupled state ^{1}(T…T), as suggested recently.[58] Thus, the difference between the two triplet species observed in the TA data of **12** might be the electronic coupling. In this case, species 2 can be assigned to ^{1}(TT) and species 3 to ^{1}(T…T) or T_1+T_1, given that these latter two cannot be distinguished in TA. The fact that ^{1}(TT) is observed as comparably long-lived species in **12** might be due to the lower long-range

order in the thin film compared with **11**, reducing the delocalization of the ^{1}(TT) and increasing the dephasing time. Importantly, in both compounds **11** and **12**, SF proceeds faster than in pentacene and, surprisingly also in PFP.[63,73] This cannot be explained by energetics, because SF in **11** and **12** is less exothermic than in pentacene and, therefore, might be related to differences in the relative molecular arrangement.

Organic field-effect transistors

To evaluate the charge-carrier transport in the pentacene derivatives, OFETs were fabricated on a highly doped Si-wafer,

which simultaneously serves as a global gate electrode. The wafer was coated with 100 nm of SiO_2 and 40 nm of Cytop 809-M which both serve as gate insulator. The latter provides an almost ideal interface with a very low density of undesired interface states acting as trap states for charge carriers in the transistor channel. The organic semiconductor was evaporated on the prepared substrate with a nominal thickness of 30 nm. Source and drain electrodes were formed by evaporating Al through a shadow mask (contact thickness is 30 nm) yielding devices with channel widths of 1000 μm and channel lengths ranging from 50 to 200 μm. Aluminum has been chosen due to its low surface work function which is preferred for the injection of electrons into the semiconductor.

Electrical characteristics were obtained by Keithley SMUs 2400 and 2600A under nitrogen atmosphere. Devices are biased to form an electron channel, the obtained electron mobilities in the saturation regime are in the range of 2×10^{-3} cm^{2}V^{-1}s^{-1} for 1,4,9,10-tetrafluoropentacene (**11**) and about 6×10^{-2} cm^{2}V^{-1}s^{-1} for 2,3,9,10-tetrafluoropentacene (**12**) (Figure 14). For the 1,4,8,11 derivative (**10**) no lateral conductivity was observable. This is most likely due to strong island growth, which prohibits formation of a closed film at the channel interface. The devices show close to ideal TFT characteristics with only a slight hint of contact resistance which can be seen in the output characteristics (Figures S42/S43 in the Supporting Information). This effect however is already negligible at source-drain voltages over 1 V. From there on the channel governs the device characteristics.
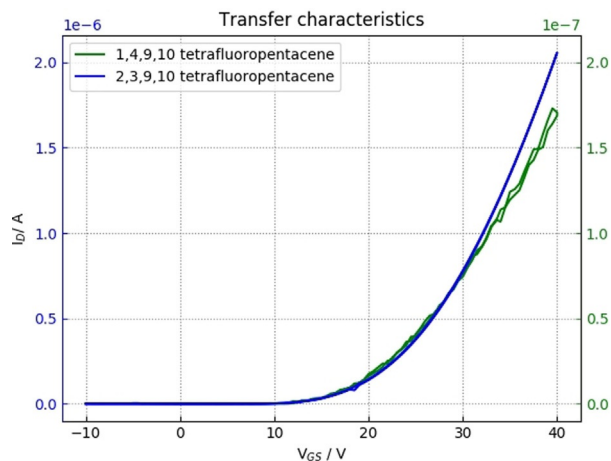
Figure 14. Transfer characteristics for 1,4,9,10-tetrafluoropentacene (**11**) and 2,3,9,10-tetrafluoropentacene (**12**). The depicted devices have a channel width of 1000 μm and channel lengths of 50 μm (2,3,9,10 tetrafluoropentacene) and 150 μm (1,4,9,10 tetrafluoropentacene), respectively. The drain-source bias is 20 V for each device. Note the difference of one order of magnitude in current between the two compounds.

Conclusions

We have performed a comprehensive comparative investigation of three tetrafluoropentacene isomers with two fluorine atoms on the terminal rings so that the dipole moment is either exactly zero or very small. We draw the following conclusions from our study:

1. The 1,2,4,5-tetrazine-induced elimination of the 6,13-etheno bridge is a good strategy for synthesis of partially fluorinated pentacenes that proceeds in good yields after minor modifications compared to our previous protocol[31] and allows easy isolation of the compounds in high purity.

2. Given that the fluorine atoms are on the two terminal rings, which have the smallest orbital coefficients in both HOMO and LUMO, it may be expected that the electronic properties are similar irrespective of the substitution patterns. We corroborated this expectation by investigation of the molecular properties using absorption and photoluminescence spectroscopy (S_0–S_1 and S_0–T_1 energy gaps), cyclic voltammetry (difference of formal potentials ΔE^0), and density functional theory (HOMO–LUMO energy gap) that all concur that the gaps are quite similar. The minor changes that are observed are due to the change of the LUMO energy, whereas the HOMO energy is hardly affected by the substitution pattern.

3. In contrast to the case of the neutral compounds, the optical gaps vary over a much larger energy range for the positively charged species, in particular for the radical cations. The EPR spectra indicate that the unpaired electron is mostly located at the central ring, and it appears that the distance of the fluorine atoms to the central ring has a significant impact on the energy of the excited state. The 1,4,8,11-isomer has the lowest energy absorption (at 1080 nm) whereas it is highest for the 2,3,9,10-isomer (920 nm). A similar trend is observed for the dications.

4. Although the molecular electronic properties of the neutral compounds are quite similar, their solid-state structures differ significantly. The 2,3,9,10- and 1,4,9,10-isomers share the herringbone packing motif with parent pentacene and perfluoropentacene, but with all four fluorine atoms at the *peri* positions (1,4,8,11-isomer, **10**) a π–π stacking motif is obtained instead. It is likely that the change in packing is due to unfavorable fluorine–π-interactions. Based on the characterization of Disiraju and Gavezzotti[74] the packing of **10** is that of the β motif due to the short axis of $a = 3.78$ Å.

5. The three isomers differ also in their chemical reactivity, because **10** readily undergoes a Woodward–Hoffmann forbidden [4+4] dimerization during NMR measurements at elevated temperatures. This is not the case for **12**, whereas **11** seems to be intermediate in reactivity so that its dimer could not be isolated. This increased reactivity does not appear to be due to decreased thermodynamic stability of **10**, because this is the most stable isomer among the series based on DFT computations (**11** and **12** are higher by 3 and 6 kcal mol^{-1}, respectively). It could however be associated with the high tendency of **10** to form noncovalent stacked dimers in the solid state that are also the immediate precursors to the transition state of thermal [4+4] dimerization according to computations reported for pentacene.[75] We feel that this difference in reactivity requires further detailed experimental and computational analysis that we plan to perform in due course.

6. Differences in crystal-structure packing may have an immediate impact on the properties of molecular films that are

of technological relevance. For example, pronounced island formation of **10** precludes its application in OFET devices, and hence the large charge-carrier mobility predicted based on computations[23] could not be experimentally confirmed. In contrast, isomers **11** and more so **12** show reasonably good n-channel semiconducting properties with charge carrier mobility up to 6×10^{-2} cm^{2}V^{-1}s^{-1}. Note that the crystal structure of **12** is most similar to that of parent pentacene.[33]

7. The two compounds crystallizing in the herringbone motif (**11**, **12**) still behave differently because films of **12** are amorphous. Nonetheless, both compounds undergo singlet fission, on a slightly shorter timescale as compared to pentacene. For **12** an additional species is observed in the TA-data, possibly a spin entangled, electronic decoupled state ^{1}(T…T).

We therefore believe that the variation of the fluorination degree and fluorination pattern of pentacene may provide a useful model for gaining detailed insight into forces that control crystallization and for studying the structure–property relationships of these organic semiconductors.

Acknowledgements

Conflict of interest

The authors declare no conflict of interest.

Keywords: acenes · organic field-effect transistors · organic semiconductors · singlet fission · synthesis

[1] H. T. Yi, M. M. Payne, J. E. Anthony, V. Podzorov, *Nat. Commun.* **2012**, *3*, 1259.
[2] M. Yi, J. Guo, W. Li, L. Xie, Q. Fan, W. Huang, *RSC Adv.* **2015**, *5*, 95273.
[3] C.-a. Di, F. Zhang, D. Zhu, *Adv. Mater.* **2013**, *25*, 313.
[4] K. N. Houk, P. S. Lee, M. Nendel, *J. Org. Chem.* **2001**, *66*, 5517.
[5] J. E. Anthony, *Chem. Rev.* **2006**, *106*, 5028.
[6] J. E. Anthony, *Angew. Chem. Int. Ed.* **2008**, *47*, 452; *Angew. Chem.* **2008**, *120*, 460.
[7] Y. Yamashita, *Sci. Technol. Adv. Mater.* **2009**, *10*, 024313.
[8] B. K. Kaushik, B. Kumar, S. Prajapati, P. Mittal, *Organic Thin-Film Transistor Applications: Materials to Circuits*, CRC, **2016**.
[9] O. D. Jurchescu, J. Baas, T. T. M. Palstra, *Appl. Phys. Lett.* **2004**, *84*, 3061.
[10] Y. Sakamoto, T. Suzuki, M. Kobayashi, Y. Gao, Y. Fukai, Y. Inoue, F. Sato, S. Tokito, *J. Am. Chem. Soc.* **2004**, *126*, 8138.
[11] C. R. Swartz, S. R. Parkin, J. E. Bullock, J. E. Anthony, A. C. Mayer, G. G. Malliaras, *Org. Lett.* **2005**, *7*, 3163.
[12] J. T. E. Quinn, J. Zhu, X. Li, J. Wang, Y. Li, *J. Mater. Chem. C* **2017**, *5*, 8654.
[13] A. Naibi Lakshminarayana, A. Ong, C. Chi, *J. Mater. Chem. C* **2018**, *6*, 3551.
[14] Y. Inoue, Y. Sakamoto, T. Suzuki, M. Kobayashi, Y. Gao, S. Tokito, *Jpn. J. Appl. Phys.* **2005**, *44*, 3663.
[15] O. D. Jurchescu, M. Feric, B. Hamadani, D. Mourey, S. Subramanian, B. Purushothaman, J. Anthony, T. Jackson, D. Gundlach, *ECS Trans.* **2008**, *16*, 283.
[16] J. B. Sherman, B. Purushothaman, S. R. Parkin, C. Kim, S. Collins, J. Anthony, T.-Q. Nguyen, M. L. Chabinyc, *J. Mater. Chem. A* **2015**, *3*, 9989.
[17] C.-H. Kim, H. Hlaing, M. M. Payne, S. R. Parkin, J. E. Anthony, I. Kymissis, *ChemPhysChem* **2015**, *16*, 1251.
[18] M. L. Tang, A. D. Reichardt, N. Miyaki, R. M. Stoltenberg, Z. Bao, *J. Am. Chem. Soc.* **2008**, *130*, 6064.
[19] M. L. Tang, A. D. Reichardt, P. Wei, Z. Bao, *J. Am. Chem. Soc.* **2009**, *131*, 5264.
[20] J. M. Wasikiewicz, L. Abu-Sen, A. B. Horn, J. M. Koelewijn, A. V. S. Parry, J. J. Morrison, S. G. Yeates, *J. Mater. Chem. C* **2016**, *4*, 7309.
[21] K. Toyoda, I. Hamada, S. Yanagisawa, Y. Morikawa, *Org. Electron.* **2011**, *12*, 295.
[22] K. Toyoda, I. Hamada, K. Lee, S. Yanagisawa, Y. Morikawa, *J. Phys. Chem. C* **2011**, *115*, 5767.
[23] V. Lukeš, D. Cagardová, M. Michalík, P. Poliak, *Synth. Met.* **2018**, *240*, 67.
[24] H.-Y. Chen, I. Chao, *ChemPhysChem* **2006**, *7*, 2003.
[25] B. Milián Medina, J. E. Anthony, J. Gierschner, *ChemPhysChem* **2008**, *9*, 1519.
[26] N. Koch, A. Gerlach, S. Duhm, H. Glowatzki, G. Heimel, A. Vollmer, Y. Sakamoto, T. Suzuki, J. Zegenhagen, J. P. Rabe, F. Schreiber, *J. Am. Chem. Soc.* **2008**, *130*, 7300.
[27] K. Reichenbächer, H. I. Süss, J. Hulliger, *Chem. Soc. Rev.* **2005**, *34*, 22.
[28] W. A. Ogden, S. Ghosh, M. J. Bruzek, K. A. McGarry, L. Balhorn, V. Young, L. J. Purvis, S. E. Wegwerth, Z. Zhang, N. A. Serratore, C. J. Cramer, L. Gagliardi, C. J. Douglas, *Cryst. Growth Des.* **2017**, *17*, 643.
[29] C.-T. Chien, T.-C. Chiang, M. Watanabe, T.-H. Chao, Y. J. Chang, Y.-D. Lin, H.-K. Lee, C.-Y. Liu, C.-H. Tu, C.-H. Sun, T. J. Chow, *Tetrahedron Lett.* **2013**, *54*, 903.
[30] C.-T. Chien, M. Watanabe, T. J. Chow, *Tetrahedron* **2015**, *71*, 1668.
[31] R. P. Bula, I. M. Oppel, H. F. Bettinger, *J. Org. Chem.* **2012**, *77*, 3538.
[32] J. Strating, B. Zwanenburg, A. Wagenaar, A. C. Udding, *Tetrahedron Lett.* **1969**, *10*, 125.
[33] B. Shen, T. Geiger, R. Einholz, F. Reicherter, S. Schundelmeier, C. Maichle-Mössmer, B. Speiser, H. F. Bettinger, *J. Org. Chem.* **2018**, *83*, 3149.
[34] M. Suzuki, T. Aotake, Y. Yamaguchi, N. Noguchi, H. Nakano, K.-i. Nakayama, H. Yamada, *J. Photochem. Photobiol. C* **2014**, *18*, 50.
[35] S.-A. Savu, G. Biddau, L. Pardini, R. Bula, H. F. Bettinger, C. Draxl, T. Chassé, M. B. Casu, *J. Phys. Chem. C* **2015**, *119*, 12538.
[36] S.-A. Savu, A. Sonström, R. Bula, H. F. Bettinger, T. Chassé, M. B. Casu, *ACS Appl. Mater. Interfaces* **2015**, *7*, 19774.
[37] A. Franco-Cañellas, Q. Wang, K. Broch, B. Shen, A. Gerlach, H. F. Bettinger, S. Duhm, F. Schreiber, *Phys. Rev. Materials* **2018**, *2*, 044002.
[38] R. Gabioud, P. Vogel, *Tetrahedron* **1980**, *36*, 149.
[39] R. Gabioud, P. Vogel, *Helv. Chim. Acta* **1983**, *66*, 1134.
[40] Y. Tsuchido, T. Ide, Y. Suzaki, K. Osakada, *Bull. Chem. Soc. Jpn.* **2015**, *88*, 821.
[41] H. Yoshio, S. Takaaki, K. Hiroshi, *Chem. Lett.* **1983**, *12*, 1211.
[42] J. M. Medina, J. L. Mackey, N. K. Garg, K. N. Houk, *J. Am. Chem. Soc.* **2014**, *136*, 15798.
[43] C. Tönshoff, H. F. Bettinger, *Chem. Eur. J.* **2012**, *18*, 1789.
[44] D. L. Boger, R. S. Coleman, J. S. Panek, F. X. Huber, J. Sauer, *J. Org. Chem.* **1985**, *50*, 5377.
[45] D. L. Boger, J. S. Panek, M. Patel, *Org. Synth.* **1992**, 79.
[46] D. Sparfel, F. Gobert, J. Rigaudy, *Tetrahedron* **1980**, *36*, 2225.
[47] T. Geiger, A. Haupt, C. Maichle-Mössmer, C. Schrenk, A. Schnepf, H. F. Bettinger, *J. Org. Chem.* **2019**, *84*, 10120.
[48] R. Einholz, T. Fang, R. Berger, P. Grüninger, A. Früh, T. Chassé, R. F. Fink, H. F. Bettinger, *J. Am. Chem. Soc.* **2017**, *139*, 4435.
[49] S. Li, Z. Li, K. Nakajima, K.-i. Kanno, T. Takahashi, *Chem. Asian J.* **2009**, *4*, 294.
[50] B. Pal, B.-C. Lin, M. V. C. dela Cerna, C.-P. Hsu, C.-H. Lin, *J. Org. Chem.* **2016**, *81*, 6223.
[51] R. S. Nicholson, *Anal. Chem.* **1966**, *38*, 1406.
[52] V. Barone, in *Recent Advances in Density Functional Methods* (Ed.: D. P. Chong), World Scientific, **1995**, pp. 287.
[53] A. R. Rakitin, D. Yff, C. Trapp, *J. Phys. Chem. A* **2003**, *107*, 6281.

[54] R. D. Pensack, A. J. Tilley, S. R. Parkin, T. S. Lee, M. M. Payne, D. Gao, A. A. Jahnke, D. G. Oblinsky, P.-F. Li, J. E. Anthony, D. S. Seferos, G. D. Scholes, *J. Am. Chem. Soc.* **2015**, *137*, 6790.

[55] R. D. Pensack, E. E. Ostroumov, A. J. Tilley, S. Mazza, C. Grieco, K. J. Thorley, J. B. Asbury, D. S. Seferos, J. E. Anthony, G. D. Scholes, *J. Phys. Chem. Lett.* **2016**, *7*, 2370.

[56] M. B. Smith, J. Michl, *Chem. Rev.* **2010**, *110*, 6891.

[57] M. K. Gish, N. A. Pace, G. Rumbles, J. C. Johnson, *J. Phys. Chem. C* **2019**, *123*, 3923.

[58] K. Miyata, F. S. Conrad-Burton, F. L. Geyer, X. Y. Zhu, *Chem. Rev.* **2019**, *119*, 4261.

[59] H. Kim, P. M. Zimmerman, *Phys. Chem. Chem. Phys.* **2018**, *20*, 30083.

[60] N. Alagna, J. Han, N. Wollscheid, J. L. Perez Lustres, J. Herz, S. Hahn, S. Koser, F. Paulus, U. H. F. Bunz, A. Dreuw, T. Buckup, M. Motzkus, *J. Am. Chem. Soc.* **2019**, *141*, 8834.

[61] L. Shen, X. Wang, H. Liu, X. Li, *Phys. Chem. Chem. Phys.* **2018**, *20*, 5795.

[62] I. Papadopoulos, J. Zirzlmeier, C. Hetzer, Y. J. Bae, M. D. Krzyaniak, M. R. Wasielewski, T. Clark, R. R. Tykwinski, D. M. Guldi, *J. Am. Chem. Soc.* **2019**, *141*, 6191.

[63] K. Kolata, T. Breuer, G. Witte, S. Chatterjee, *ACS Nano* **2014**, *8*, 7377.

[64] M. J. Y. Tayebjee, K. N. Schwarz, R. W. MacQueen, M. Dvořák, A. W. C. Lam, K. P. Ghiggino, D. R. McCamey, T. W. Schmidt, G. J. Conibeer, *J. Phys. Chem. C* **2016**, *120*, 157.

[65] L. Wang, Y. Olivier, O. V. Prezhdo, D. Beljonne, *J. Phys. Chem. Lett.* **2014**, *5*, 3345.

[66] N. Renaud, P. A. Sherratt, M. A. Ratner, *J. Phys. Chem. Lett.* **2013**, *4*, 1065.

[67] S. Schiefer, M. Huth, A. Dobrinevski, B. Nickel, *J. Am. Chem. Soc.* **2007**, *129*, 10316.

[68] R. B. Campbell, J. M. Robertson, J. Trotter, *Acta Crystallogr.* **1962**, *15*, 289.

[69] M. W. B. Wilson, A. Rao, J. Clark, R. S. S. Kumar, D. Brida, G. Cerullo, R. H. Friend, *J. Am. Chem. Soc.* **2011**, *133*, 11830.

[70] J. J. Snellenburg, S. Laptenok, R. Seger, K. M. Mullen, I. H. M. van Stokkum, *J. Stat. Software* **2012**, *49*, 1.

[71] C. Jundt, G. Klein, B. Sipp, J. Le Moigne, M. Joucla, A. A. Villaeys, *Chem. Phys. Lett.* **1995**, *241*, 84.

[72] W.-L. Chan, M. Ligges, A. Jailaubekov, L. Kaake, L. Miaja-Avila, X.-Y. Zhu, *Science* **2011**, *334*, 1541.

[73] V. O. Kim, K. Broch, V. Belova, Y. S. Chen, A. Gerlach, F. Schreiber, H. Tamura, R. G. D. Valle, G. D'Avino, I. Salzmann, D. Beljonne, A. Rao, R. Friend, *J. Chem. Phys.* **2019**, *151*, 164706.

[74] G. R. Desiraju, A. Gavezzotti, *Acta Crystallogr. Sect. B* **1989**, *45*, 473.

[75] S. S. Zade, N. Zamoshchik, A. R. Reddy, G. Fridman-Marueli, D. Sheberla, M. Bendikov, *J. Am. Chem. Soc.* **2011**, *133*, 10803.